A Numerical Study of Near Inertial Motions in Mid-Atlantic Bight Area Induced by Hurricane Irene (2011)

Peida Han[1] and Xiping Yu[2]

Abstract

Hurricane Irene generated strong near inertial currents (NICs) in the ocean waters when passing over the Mid-Atlantic Bight (MAB) of the U. S. East Coast in late August 2011. It is demonstrated that a combination of the valuable field data with detailed model results can be exploited to study the development and decay mechanism of this event. Numerical results obtained with regional oceanic modeling system (ROMS) are shown to agree well with the field data. Both computed and observed results show that the NICs were significant in most areas of the MAB region except in the nearshore area where the stratification was totally destroyed by the hurricane-induced strong mixing. Based on the energy budget, it is clarified that the near inertial kinetic energy (NIKE) was mainly gained from the wind power during the hurricane event. In the deep water region, NIKE was basically balanced by the vertical turbulence diffusion (40%) and downward divergence (33%). While in the continental shelf region, NIKE was mainly dissipated by the vertical turbulence diffusion (67%) and partially by the bottom friction (24%). Local dissipation of NIKE due to turbulence diffusion is much more closely related to the rate of the vertical shear rather than the intensity of turbulence. The strong vertical shear at the offshore side of the continental shelf leaded to a rapid dissipation of NIKE in this region.

Keywords: Hurricane Irene (2011); Mid-Atlantic Bight; Near inertial current; Energy budget; Timescale of near inertial energy decay

[1] PhD Candidate. Department of Hydraulic Engineering, Tsinghua University, Beijing, China.

[2] Corresponding Author. Professor. Department of Ocean Science and Engineering, Southern University of Science and Technology, Shenzhen, China. Email: yuxp@sustech.edu.cn

1. Introduction

Near inertial currents (NICs), observed widely in ocean basins around the world, are characterized by the important role of Coriolis effect and by the periodic motion with the frequency of an inertial mode (Garrett, 2001). The basic energy source of these freely flowing currents is the wind power (Pollard, 1980; D'Asaro et al., 1985). Globally, the annually averaged wind power supply to NICs was estimated ranging from 0.3 TW to more than 1 TW by previous investigators (Alford, 2003a; Furuichi et al., 2008; Rimac et al., 2013). As a comparison, the total power required to maintain the abyssal stratification and the thermohaline circulation is about 2 TW (Munk and Wunsch, 1998). This implies that NIC is a very important phenomenon in physical oceanography (Gregg, 1987; Alford, 2003b; Jochum et al., 2013).

A tropical or an extratropical cyclone (hereinafter collectively referred as TC) is a rotating low-pressure and strong-wind mesoscale weather system, which generates NICs more powerfully than other types of atmospheric processes in nature (Alford et al., 2016; Steiner et al., 2017). When a TC passes over a deep ocean, enormous energy is directly transferred into the ocean waters, which rapidly generates strong NICs with a velocity up to 1 m/s in the horizontal direction of the mixed layer (Price, 1983; Sanford et al., 2011). Right-bias effect is often shown in the NIC pattern, i.e., NICs are more intense on the right side of the hurricane track, due to the resonance between the surface flow driven by NICs and clockwise rotating wind stress on the right side (Chang and Anthes, 1978; Price, 1994). After the passage of a TC, the surface near inertial energy usually persists for several inertial cycles, and then gradually decays (Price, 1983; Sanford et al., 2011; Hormann et al., 2014; Zhang et al., 2016; Wu et al., 2020).

It is known that NICs in shallow waters show some significant differences with those in deep waters and the velocity of NICs in shallow waters is usually of a smaller magnitude of 0.1-0.5 m/s (Chen and Xie, 1997; Rayson et al., 2015; Yang et al., 2015; Chen et al., 2017; Zhang et al., 2018). The decrease of current velocity in shallow waters may be an effect of the sea-bottom friction as Rayson et al. (2015) pointed out. Chen and Xie (1997), however,

found that it was because a significant part of the wind input, which may otherwise be an energy source of the NICs, was exhausted to generate a wave-induced nearshore current system. Chen et al. (2017) considered that barotropic waves in the shallow waters, such as seiches, may trap some wind energy. In addition to the difference in magnitude, the modes of the NICs in shallow and deep waters are also different. More specifically, a two-layer structure was observed in shallow waters in several studies, i.e., NICs were in opposite phases in surface and bottom layers, which differed from the conventional multi-layer mode in deep waters (Chen et al., 1996; Shearman, 2005; Yang et al., 2015), though a multi-layer mode may also be observed sometimes in nearshore waters due to combined effect of changing wind stress, variable stratification and nonlinear bottom friction (Mackinnon and Gregg, 2005).

There have been a considerable number of studies on the decay of specific TC generated NICs in coastal regions. Rayson et al. (2015) paid attention to four intense TCs on the Australian North-West Shelf and related the rapid decay of NICs in shallow waters to the bottom friction. Yang et al. (2015) examined coastal ocean responses to Typhoon Washi and found that the negative background vorticity could trap near inertial energy and result in a slow decay. Shen et al. (2017) investigated five TCs over the Taiwan Strait and identified a rapid decaying rate due to nonlinear interaction between NICs and tides. Zhang et al. (2018) studied Hurricane Arthur in Mid-Atlantic Bight and showed that excessive wind input does not necessarily lead to amplification of NICs because intensive wind input is usually accompanied by an even higher rate of energy dissipation.

Though a significant number of investigations have been conducted, some basic features of a TC induced NIC in the coastal ocean are still not clarified. For instance, the energy budget in the NIC generated by a TC has not yet been thoroughly discussed in either deep or shallow waters; and the relative importance of different physical processes including advection, conversion, turbulence diffusion, bottom friction, energy divergence, etc., in the energy budget has not yet been fully understood. In addition, it is still not concluded on which processes dominate the decay of near inertial energy or on how each physical process

affects the decay rate of the near inertial energy in deep and shallow waters, respectively. Our limited understanding to the basic features of a TC induced NIC is largely due to the difficulties in ocean observations under extreme weather.

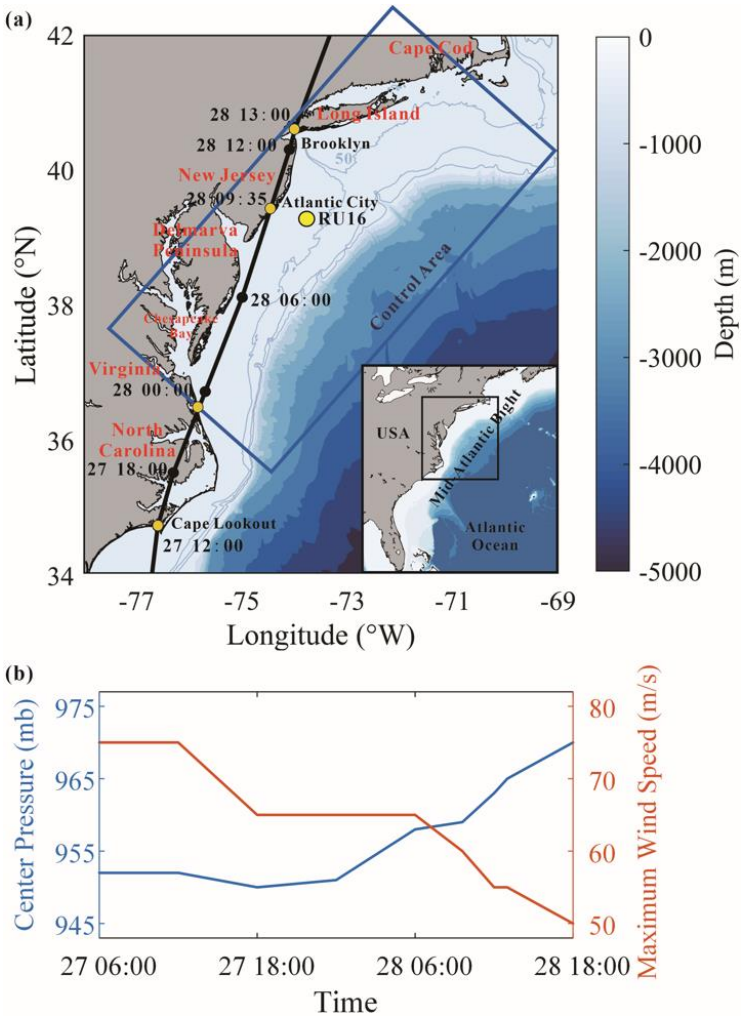

Figure 1. (a) Map of the MAB region. Best track of Hurricane Irene (2011) reported by Avila and Cangialosi (2011) is shown by a black line. Reanalysis data provided by H*WIND shows a similar track with Avila and Cangialosi (2011) and is thus omitted. The mean position of Glider RU16 is marked by a yellow circle. The control domain defined in Section 4 is marked by a blue box. (b) Time series of center pressure and 10-m maximum wind speed of Hurricane Irene reported by Avila and Cangialosi (2011).

In this study, we pay a close attention to the NIC induced by Hurricane Irene (2011). Hurricane Irene (2011) crossed over the Mid-Atlantic Bight (MAB), a coastal region of the North Atlantic, extending from Cape Cod, Massachusetts to Cape Lookout, North Carolina,

USA, as shown in Figure 1a. Before the hurricane event, seawater stratification in MAB was quite strong due to the Cold Pool effect (Lentz, 2017) and the temperature difference between the surface and the bottom exceeded 10 °C. The vertical gradient of the temperature should also be very large because previous studies showed that the thermocline in shelf region was rather thin; for instance, the thermocline was less than 5 m in the place where water depth was around 40 m (Glenn et al., 2016; Seroka et al., 2017). During the passage of Hurricane Irene (2011), a network of High-frequency (HF) radars measured the surface currents in MAB (Roarty et al., 2010). Meanwhile, a Slocum glider launched near New Jersey measured the vertical profiles of the temperature and the salinity (Schofield et al., 2010). Combination of the valuable field data with effective numerical techniques then provided an opportunity to achieve a comprehensive study of the NICs generated by this hurricane event.

2. Numerical Model

2.1 Basic Equations

In this study, the ocean responses to Hurricane Irene (2011) are studied using the regional oceanic modeling system (ROMS) (Shchepetkin and McWilliams, 2005; Haidvogel et al., 2008). ROMS deals with the Reynolds-averaged N-S equations in the σ coordinate system (Freeman et al., 1972). Specifically, the Cartesian coordinate z is replaced by σ based on a general relation $\chi\ \sigma\ =\ z-\eta\ /\ D$, where η is the vertical displacement of the free surface and D is the instantaneous water depth, while $\chi\ \sigma$ is a stretching function introduced for grid refinement. In the σ-coordinate system the Reynolds-averaged N-S equations may finally be expressed as

$$\frac{\partial \xi}{\partial t}+\frac{\partial\ \xi u}{\partial x}+\frac{\partial\ \xi v}{\partial y}+\frac{\partial\ \xi \omega}{\partial \sigma}=0 \tag{1}$$

$$\frac{\partial\ \xi u}{\partial t}+\frac{\partial\ \xi uu}{\partial x}+\frac{\partial\ \xi uv}{\partial y}+\frac{\partial\ \xi u\omega}{\partial\sigma}-f\xi v+\frac{\xi}{\rho}\frac{\partial p}{\partial x}$$
$$=-g\xi\left(\chi\frac{\partial D}{\partial x}+\frac{\partial\eta}{\partial x}\right)+\frac{\partial}{\partial\sigma}\left(\frac{\nu}{\xi}\frac{\partial u}{\partial\sigma}\right)+\frac{\partial}{\partial x}\left(\xi\nu'\frac{\partial u}{\partial x}\right)+\frac{\partial}{\partial y}\left(\xi\nu'\frac{\partial u}{\partial y}\right) \tag{2}$$

$$\frac{\partial\ \xi v}{\partial t}+\frac{\partial\ \xi uv}{\partial x}+\frac{\partial\ \xi vv}{\partial y}+\frac{\partial\ \xi v\omega}{\partial\sigma}+f\xi u+\frac{\xi}{\rho}\frac{\partial p}{\partial y}$$
$$=-g\xi\left(\chi\frac{\partial D}{\partial y}+\frac{\partial\eta}{\partial y}\right)+\frac{\partial}{\partial\sigma}\left(\frac{\nu}{\xi}\frac{\partial v}{\partial\sigma}\right)+\frac{\partial}{\partial x}\left(\xi\nu'\frac{\partial v}{\partial x}\right)+\frac{\partial}{\partial y}\left(\xi\nu'\frac{\partial v}{\partial y}\right) \tag{3}$$

$$0=-\frac{1}{\rho}\frac{\partial p}{\partial\sigma}-g\xi \tag{4}$$

$$\frac{\partial\ \xi C}{\partial t}+\frac{\partial\ \xi uC}{\partial x}+\frac{\partial\ \xi vC}{\partial y}+\frac{\partial\ \xi\omega C}{\partial\sigma}$$
$$=\frac{\partial}{\partial\sigma}\left(\frac{\kappa}{\xi}\frac{\partial C}{\partial\sigma}\right)+\frac{\partial}{\partial x}\left(\xi\kappa'\frac{\partial C}{\partial x}\right)+\frac{\partial}{\partial y}\left(\xi\kappa'\frac{\partial C}{\partial y}\right) \tag{5}$$

where, $\xi=\partial z/\partial\sigma=D\ \partial\chi/\partial\sigma$; u, v, ω are the velocity components in x, y, σ directions, respectively; C stands for the potential temperature T or salinity S; p is the seawater pressure; ρ is the density of the seawater; $f=2\Omega\sin\phi$ is the Coriolis parameter with $2\Omega=1.458\times10^{-4}\ \mathrm{s}^{-1}$ and ϕ being the latitude; ν and κ are the diffusion coefficients for momentum and potential temperature or salinity, respectively, in the vertical direction; ν' and κ' are those in the horizontal directions; Note that Eq. (1) is the continuity equation; Eqs. (2) and (3) are equations of motion in two horizontal directions; Eq. (4) is the hydrostatic assumption; Eq. (5) is the advection-diffusion equation of the potential temperature or the salinity. The density of the seawater ρ is determined following the equation of state proposed by Jackett and McDougall (1995):

$$\rho\ S,T,p\ =\frac{\rho_0}{1-p/K\ S,T,p} \tag{6}$$

where $\rho_0=\rho\ S,T,0$ is the seawater density at the standard atmospheric pressure and $K\ S,T,p$ is the bulk modulus, both are given by Jackett and McDougall (1995).

The vertical mixing is known to play an important role in determining the structure of a NIC, so it must be properly evaluated. In this study, we consider $\nu=\nu_0+\nu_e$ and

$\kappa = \kappa_0 + \kappa_e$, in which ν_0 and κ_0 are the molecular viscosity and diffusivity of the seawater, set to $\nu_0 = 10^{-5}\,\mathrm{m^2/s}$ and $\kappa_0 = 10^{-6}\,\mathrm{m^2/s}$ following previous suggestions (Xu et al., 2002; Li and Zhong, 2007; Lentz, 2017), while ν_e and κ_e are the eddy viscosity and diffusivity, determined by the conventional k-ε turbulence model (see Rodi (1987) and Umlauf and Burchard (2003) for detailed description), a widely employed model that demonstrated good performance in simulating various oceanographic processes (Olabarrieta et al., 2011; Toffoli et al., 2012; Zhang et al., 2018).

Horizontal mixing is included in Eqs. (2), (3) and (5), though it has been pointed out to play a relatively insignificant role in simulating response of the stratified ocean to a hurricane, as compared to vertical mixing (Li and Zhong, 2007; Zhai et al., 2009; Dorostkar et al., 2010). In the ocean basin of the present interest, the horizontal diffusion coefficient was estimated to be an order of 10 $\mathrm{m^2/s}$ under extreme conditions, e.g., TC condition (Allahdadi, 2014; Mulligan and Hanson, 2016). Thus, we take $\nu' = \kappa' = 10\,\mathrm{m^2/s}$ in the present study for simplicity to simulate the ocean response to Hurricane Irene.

2.2 Computational Conditions

In order to fully capture the NIC induced by Hurricane Irene (2011), our computational domain covers the entire MAB regions of the U. S. East Coast extending from Cape Cod, Massachusetts, to Cape Lookout, North Caroline. The computational domain is discretized into 35 layers with refinement near the surface and covered with a 5 km×5 km grid in the horizontal plane. The 1 arc-min bathymetry data is obtained from ETOPO1 Global Relief Model (Amante and Eakins, 2009) and resampled to a resolution of 5 km. The simulation starts from 20 August, one week before the hurricane event and lasted for a period of 16 days. The time step is set to 1 min.

The initial and open boundary conditions of the seawater temperature and salinity, the ocean flow velocities and the sea surface elevation are all from the Hybrid Coordinate Ocean Model (HYCOM, https://www.hycom.org/) with a resolution of 1/12° in space and 3 hr in time (Cummings, 2005; Chassignet et al., 2007). The initial stratification in the HYCOM is examined through a comparison with the 4D data provided by Experimental System for

Predicting Shelf and Slope Optics (ESPreSSO, http://www.myroms.org/espresso/). Seven tidal constitutes (M2, S2, N2, K2, O1, K1, Q1) included in the simulation are derived from the ADvanced CIRCulation model (ADCIRC, https://adcirc.org/). Daily inflows from the eleven largest rivers, containing Susquehanna River, Delaware River, Hudson River, Potomac River, etc., are obtained from the United States Geological Survey (USGS, https://waterdata.usgs.gov/). The so-called radiation-nudging condition is adopted at the open boundaries (Marchesiello et al., 2001). Wet-and-dry option is activated at coastal boundaries (Warner et al., 2013). The seabed boundary condition is required to satisfy:

$$\nu \frac{\partial \mathbf{u}}{\partial z} = \boldsymbol{\tau}_{\mathrm{b}} = \rho \left[\frac{\lambda}{\ln\ \Delta z / z_0} \right]^2 \left| \mathbf{u}_{\mathrm{b}} \right| \mathbf{u}_{\mathrm{b}} \tag{7}$$

where, $\boldsymbol{\tau}_{\mathrm{b}}$ is the bottom friction; λ is the von Karman constant; $\mathbf{u}_{\mathrm{b}}$ is the fluid velocity at the center of the bottom layer; Δz is the distance between the center of the bottom layer and the seabed; z_0 is the bottom roughness, which is set to 0.02 m in MAB following Churchill et al. (1994).

The hurricane wind forcing required in this study can be obtained from two sources, i.e., the H*WIND data, with a spatial resolution of 6 km and a temporal resolution of 6 hr, published by Atlantic Oceanographic and Meteorological Laboratory, National Oceanic and Atmospheric Administration (AOML/NOAA) (https://www.aoml.noaa.gov/hrd/data_sub/wind.html) (Powell et al., 1998) and the North American Mesoscale (NAM) data, with a spatial resolution of 12 km and a temporal resolution of 3 hr, provided by National Centers for Environmental Prediction (NCEP) (https://www.ncdc.noaa.gov/data-access/model-data/model-datasets/north-american-mesoscale-forecast-system-nam) (Janjic et al., 2004). In our computation, the former is used between 26 and 31 August (during the hurricane event) because it has a better accuracy in capturing the maximum wind speed, while the latter is used during other periods of the simulation. Reanalysis data for other atmospheric forcing, such as the surface air temperature, air pressure, relative humidity, radiation and precipitation are also available from NAM for determining the surface buoyancy fluxes. In particular, the wind drag τ_s, which is measure of the momentum flux can be estimated

through (Fairall et al., 1996):

$$\tau_s = \rho_a C_d u_{10}^{\ 2} \tag{8}$$

where, ρ_a is the density of the air; C_d is the drag coefficient; u_{10} is the horizontal wind speed at the 10-m level; Several studies have confirmed that C_d does not increase but level off or even decrease at high wind speeds (Emanuel, 1995; Powell et al., 2003; Donelan et al., 2004). Besides, C_d could be altered due to wave deformation in response to bathymetry change, especially in coastal regions (Chen et al., 2018; Xu and Yu, 2021). In order to correctly represent the effect of the air-sea interactions under extreme wind conditions, we choose an empirical formula which fits the numerical results obtained with the improved wave boundary layer model developed by Chen and Yu (2016), Chen et al. (2018) and Xu and Yu (2021):

$$C_d = C_{dw} + \frac{C_{d0} - C_{dw}}{(W_0 - W)^2}(u_{10} - W)^2 \tag{9}$$

where C_{d0} is a threshold value set to 0.001 for the wind stress at $u_{10} \le W_0 = 5$ m/s, C_{dw} is the saturated wind stress coefficient and W is the saturation wind speed. We have

$$C_{dw} = \begin{cases} -1.86\times10^{-4}\ln\dfrac{gD}{W_D} + 0.0025 & \dfrac{gD}{W_D} \le 3 \\ 0.00225 & \dfrac{gD}{W_D} > 3 \end{cases} \tag{10}$$

$$W = \begin{cases} 4.64\ln(\dfrac{gD}{W_D}) + 42.6 & \dfrac{gD}{W_D} \le 0.6 \\ W_D & \dfrac{gD}{W_D} > 0.6 \end{cases} \tag{11}$$

where W_D set to 40 m/s is the saturation wind speed in deep water. Except for the momentum flux, other air-sea fluxes, e.g., the sensible heat flux and the latent heat flux, are determined based on the conventional bulk parameterization scheme (see Fairall et al. (1996) for detailed description). The sea surface boundary condition is then required to satisfy:

$$\nu \frac{\partial \mathbf{u}}{\partial z} = \boldsymbol{\tau}_s \tag{12}$$

2.3 Observational data

During the passage of Hurricane Irene (2011), a network of High-frequency (HF) radars measured the surface currents and a Slocum glider launched near New Jersey measured the vertical profiles of the temperature and the salinity (Roarty et al., 2010; Schofield et al., 2010). The measured data are used to verify the computational results in this study. In fact, they have been widely used in previous studies (Glenn et al., 2016; Seroka et al., 2016; Seroka et al., 2017).

HF Radars in the Mid-Atlantic Regional Association's Coastal Ocean Observing System (MARACOOS, https://maracoos.org/) are able to observe the surface currents. The recorded data have a temporal resolution of 1 hr and a spatial resolution of 6 km, and are assumed to be measured at an effective depth of around 2.7 m below the ocean surface based on Roarty et al. (2020). The data cover the MAB area from the coast to the shelf break and have a reasonably good accuracy. In fact, they show a RMS difference within 8 cm/s when compared with data measured by ADCP (Roarty et al., 2010; Roarty et al., 2020).

Glider RU16 was an autonomous underwater vehicle of the Rutgers Slocum glider (Schofield et al., 2007, 2010) platform developed by Teledyne-Webb Research (https://rucool.marine.rutgers.edu/data/underwater-gliders), and has demonstrated to be advantageous in marine monitoring, particularly under extreme weather conditions (Glenn et al., 2016; Miles et al., 2017; Seroka et al., 2016; Seroka et al., 2017; Zhang et al., 2018). It was equipped with the Seabird un-pumped conductivity, temperature, and depth (CTD) sensor, and could thus measure not only the vertical profiles of the seawater temperature and the salinity but also the water depth. It was programmed to move vertically through the water column, collect data every 2 s, and surface at a 3 h interval to provide high temporal resolution data (Schofield et al., 2007; Glenn et al., 2016; Seroka et al., 2016).

3 Ocean Responses to Hurricane Irene

3.1 Effect of hurricane on ocean surface flow

As shown in Figure 1, Hurricane Irene (2011) entered the Mid-Atlantic Bight (MAB)

area of the present interest at Cape Lookout, North Carolina as a Category-1 event at 12:00, 27 August, 2011 (UTC time, the same below) with a maximum sustained wind (MSW) of over 38 m/s. It continued to move northeastward and made a landfall at Atlantic City, New Jersey at 9:35, 28 August with a MSW of around 30 m/s. During its motion in the MAB area of our interest, the radius of the hurricane wind field (the area with wind speed $\geqslant$32.9 m/s) reached a large value of 140 km (Avila and Cangialosi, 2011).

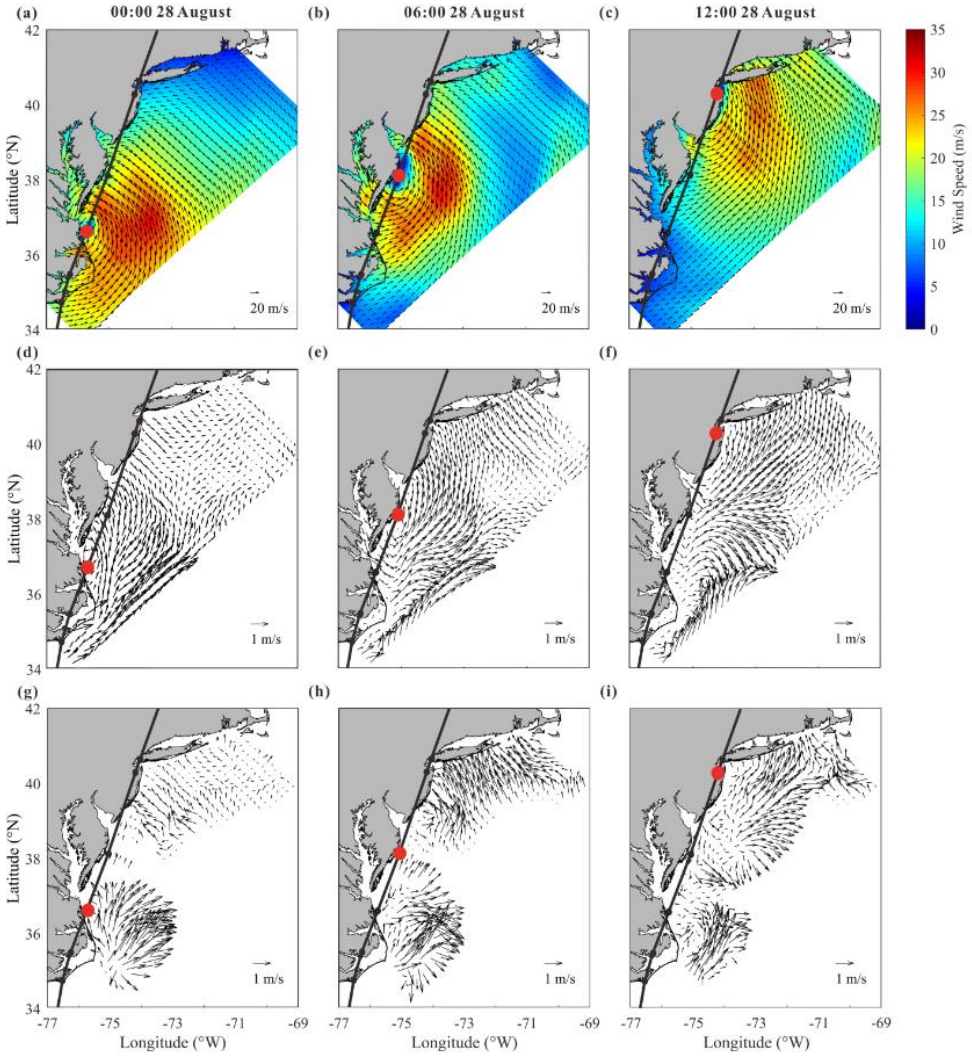

Figure 2. Snapshots of (a-c) the 10-m wind provided by H*WIND, (d-f) computed current velocity of the surface layer and (g-i) observed current velocity of the surface layer, at (left column) 00:00, (middle column) 06:00 and (right column) 12:00, 28 August, during the passage of Hurricane Irene (2011). Note that best track of the hurricane reported by Avila and Cangialosi (2011) is shown by black lines while the hurricane center is shown by red circles.

Figure 2 provides the snapshots of the wind, the computed and observed currents in the MAB area at 00:00, 06:00 and 12:00, 28 August, 2011, respectively. Note that 00:00 and 12:00 correspond to the time when Hurricane Irene entered and left the area of our interest, respectively. The wind field is plotted from the H*WIND data, while the field currents are obtained from the HF Radars and detided.

The computed current velocity of the surface layer, as shown in Figure 2d-f, is compared with the observed one, as shown in Figure 2g-i, to verify the reliability of the numerical model presented in this study. At 00:00, 28 August, it is numerically demonstrated that currents rotating counterclockwise with a magnitude of over 1 m/s are rapidly generated by the wind near the hurricane center (Figure 2d). In the observed results, though there are significant data missing near the hurricane center, northeastward currents can still be identified on the offshore waters along North Carolina coast (Figure 2g) and are in reasonable agreement with the computed current field. Moreover, both computational and observational results support a fact that the onshore wind (Figure 2a) on the front side of the hurricane drives an onshore current with magnitude of 0.4 m/s along the northern MAB, especially in the nearshore area of New Jersey (Figure 2d and 2g). At 06:00, Hurricane Irene arrived at the offshore waters of Delmarva Peninsula. In spite of the field data missing, the rotating currents induced by the hurricane wind can be clearly recognized in both computed and observed results in the nearshore area of New Jersey (Figure 2e and 2h). In addition, relatively strong onshore currents with magnitude of over 1 m/s are observed near Long Island and are also well represented in the numerical results (Figure 2e). At 12:00, i.e., the time when the hurricane left the area of our interest, the counterclockwise rotating currents are still formed near the hurricane center as demonstrated by both computational and observational results (Figure 2f and 2i). At the same time, clockwise rotating currents are shown to be generated near Delmarva Peninsula in southern MAB after the hurricane passed over. This fact is certainly confirmed by both computed and observed results, indicating near inertial currents are activated after the hurricane event. Therefore, it becomes evident that the rotating wind of the hurricane immediately forces a rotating current in the surface

layer of the ocean and induces an inertial current rotating in the opposite direction shortly after the hurricane passed over. It is also worthwhile to emphasize that, in general, the numerical results obtained with the present model agree fairly well with observed data.

3.2 Effect of hurricane on vertical stratification and sea surface cooling

Shown in Figure 3a is the vertical profile of the seawater temperature measured by Glider RU16 launched off the New Jersey Coast. In Figure 3a, it is seen that the mixed layer off New Jersey coast was quite thin, with a thickness of less than 10 m, before the hurricane event. A strong stratification was clearly formed over a water depth of 40 m, with a surface temperature of 24 °C and a bottom temperature of 10 °C. When the hurricane center passed over the position of Glider RU16 at around 09:30, 28 August, the thickness of the mixed layer rapidly increased to nearly 30 m while the surface temperature was decreased by more than 5 °C, indicating a strong mixing process has occurred. By plotting the time series of the squared buoyancy frequency N based on the measured data, expansion of the mixed layer due to the hurricane event may be more vividly demonstrated (Figure 3c).

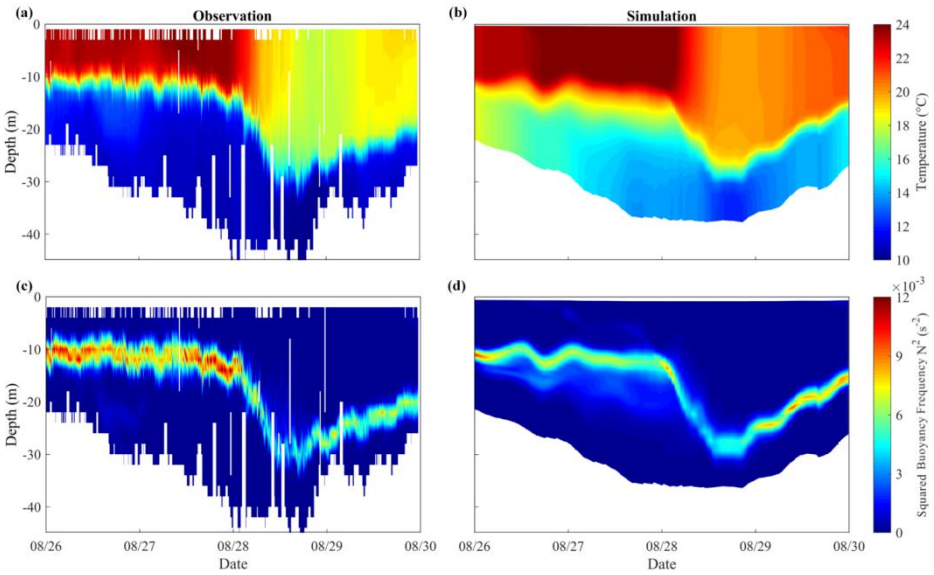

Figure 3. Time series of the vertical profiles of (top row) the temperature and (bottom row) the squared buoyancy frequency, obtained from (a, c) Glider RU16 and (b, d) numerical model.

Figure 3b and 3d present the computed results for the vertical distribution of seawater temperature obtained by virtually setting a measuring point moving with the glider in the real situation. The numerical results show a similar variation of the stratification pattern before and during the hurricane event, indicating that the numerical model is capable of describing the development and destruction of ocean stratification. However, a sea surface cooling of about 4 °C obtained by the numerical model is a little smaller than 6-7 °C observed by the glider in the field, probably due to the inaccurate setting of the initial bottom temperature in the computation. Discrepancies of the squared buoyancy frequency N was also found in the thermocline (Figure 3c), where the temperature varied most dramatically. They are probably caused by the inaccurate setting of the initial temperature profile. In fact, the initial condition for the bottom temperature in HYCOM is somehow higher (about 4°C) than the observed value in the field if Figures 3a and 3b are compared. To correct this system error, the real-time profile obtained from RU16 is used for a nudging process in computation, i.e., the model temperature and salinity fields are forced to nudge toward observed data (see Thyng et al. (2021) for detailed description).

The sea surface temperatures (SST) before and after the hurricane event are further compared in Figure 4 (obtained from The Advanced Very High Resolution Radiometer (AVHRR), https://earth.esa.int/eogateway/catalog/avhrr-level-1b-local-area-coverage-imagery). Before the hurricane event, both observed and computed SST show similar patterns, i.e., the SST decreases with the increasing latitude. After the hurricane passage, the strong mixing and cooling mainly take place in shallow waters, where the initial stratification is strong (Zhang et al., 2016), especially near New Jersey and Long Island. However, the cooling is not prominent in shallow waters near North Carolina. In fact, it has been reported that the SST in this region had decreased and then recovered to its pre-hurricane level within only 1 day (Seroka et al., 2016). The HYCOM data showed that the initial bottom temperature near North Carolina was as high as 18 °C. Therefore, little Cold Pool water in this region may have caused insignificant cooling and fast recovering.

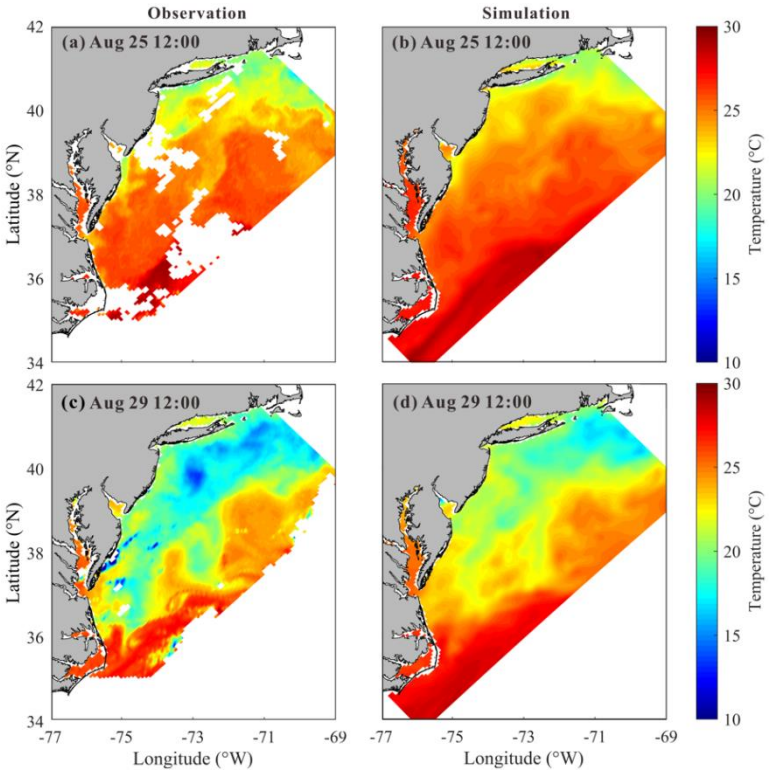

Figure 4. Sea surface temperature at Aug 25 12:00, before the hurricane event (top row) and at Aug 29 12:00, after the hurricane event (bottom row) from (a, c) observed data and (b, d) numerical model.

It should be pointed out that the computed SST cooling is 3-4 °C smaller than the observed one, which could also be explained by the inaccurate initial condition obtained from HYCOM. The HYCOM bottom temperature is somehow higher than actual, which could lead to the underestimation of the SST cooling. Therefore, we use the real-time SST data obtained from AVHRR for nudging process in computation to correct this system error (Thyng et al., 2021), considering that the accuracy of the initial stratification could obviously affect the modeling of mixing process. Note that the error is mainly caused by the discrepancy in initial settings but not the defects in numerical method. Thus this error could be calibrated in certain extent and thus would not affect the reliability of subsequent analysis, e.g. energy budget analysis.

3.3 Characteristics of NIC

To have a general understanding of the NICs in the MAB area induced by Hurricane Irene (2011), a network of 30 stations aligned on 5 cross-shore sections from south to north is introduced in this study to cover the area of our interest as shown in Figure 5, similar to Zhang et al (2018). In each section, 6 stations are placed in the cross-shore direction from the shore side to the deep ocean, where water depths are around 30 m, 50 m, 75 m, 120 m, and 220 m and 1000 m, respectively. Note that the most offshore stations are located outside the shelf break.

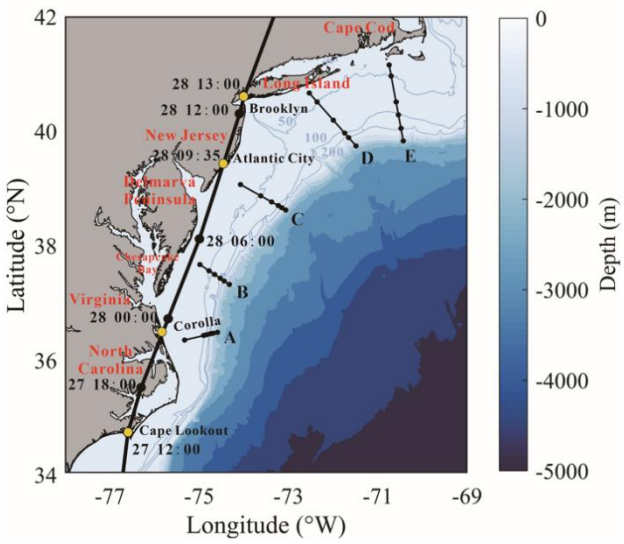

Figure 5. Five virtual sections marked by short black lines.

The velocity of NIC is obtained from the total current velocity by first excluding the tidal components and then passing it through a Butterworth filter with the frequency band of 0.8-1.2 f_0, an effective approach proposed by Hormann et al. (2014), Zhang et al. (2018) and Kawaguchi et al. (2020). Shown in Figure 6 are the time series of surface velocity of the NIC component in the cross-shore direction at all stations during the time period of our study (16 days from 20 August to 5 September). The alongshore component was similar to cross-shore component and thus omitted here. It is demonstrated that the numerical results are in reasonably good agreement with the HF Radar data and the Pearson product-moment correlation coefficient reaches 0.7 (Derrick et al., 1994). The major sources of error in the measured data are found at the most offshore stations, such as A6 and D6, where the

coverage of HF Radar is limited, i.e., at around 50 % (Roarty et al., 2010; Kohut et al. 2012). Previous studies indicated that the observed data outside the shelf break with such a low coverage should be used with caution (Roarty et al., 2010; Kohut et al. 2012; Roarty et al. 2020). Error in the numerical results of the NICs may come from the minor errors in the wind forcing data because they are very sensitively related, e.g., underestimation at C3-C6 before the hurricane event may come from the errors in low-resolution NAM data used in pre-hurricane periods.

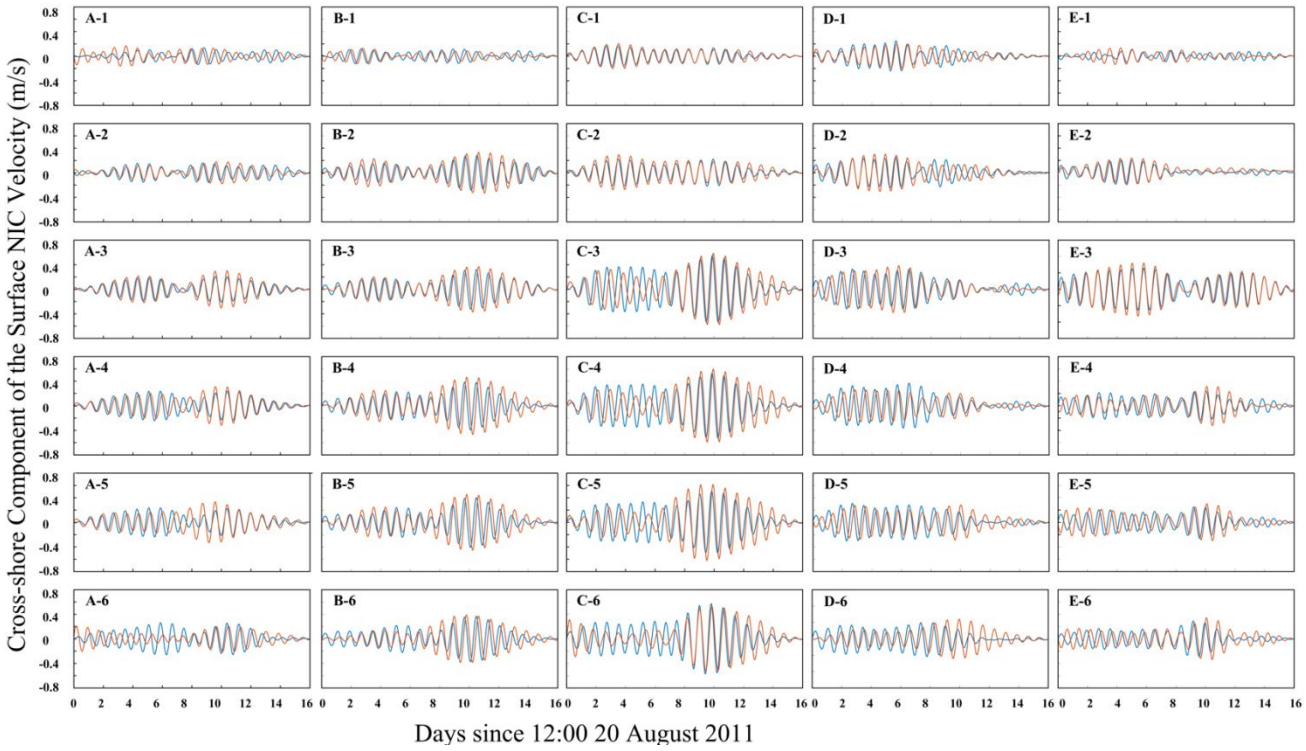

Figure 6. Time series of the NIC velocity in the surface layer obtained (blue line) by the HF Radar and (orange line) with numerical model at 30 stations along sections A-E.

In Figure 6, it can be readily recognized that, in the cross-shore direction from shallow to deep waters (i.e., Station No.1-No.5 in present study), the NIC velocity gradually increases by a factor of at least three, e.g., from 0.15 m/s to 0.6 m/s in section C, which is consistent with conclusions in previous studies (Kim and Kosro, 2013; Yang et al., 2015; Rayson et al., 2015; Zhang et al., 2018). This is because that NIC velocity in the nearshore region are restricted due to a combination of several reasons presented by Chen and Xie (1997), Rayson et al. (2015) and Chen et al. (2017). Different from other studies, however,

383 the NIC velocity in the deep waters (i.e., Station No. 6 in the present study) is found to be
384 not larger or even smaller than that nearby the shelf break. This is probably due to that fact
385 that the track of Hurricane Irene (2011) was nearly attached to the shore during its motion
386 in the area of our interest and the wind stress over the deep ocean was relatively small. From
387 south to north, it is found that the NIC velocity in the middle regions, such as along section
388 C, is larger than those in south and north. By checking the numerical results, it is found that
389 the stratification was only slightly destroyed during the hurricane event near section C as
390 compared to the adjacent sections, which thus provided a better environment for NIC
391 generation (Yang et al., 2015; Shen et al., 2017).

392 To evaluate the relative importance of the near inertial currents, the rotary spectra of
393 the surface current velocity during the period of study (16 days) at different stations are
394 shown in Figure 7. The tidal flows corresponding to the major constituents M2, N2 and K1,
395 obtained with ADCIRC, are also plotted. It is seen that the velocity of the NICs is of an
396 equivalent magnitude to that of the M2 tidal current at the shallow-water stations where the
397 water depth is about 30 m (section C was taken for an example, Figure 7a). But, the velocity
398 of the NICs is significantly larger than that of the tidal current in deeper regions (Figure 7b,
399 c). It may be necessary to point out that weak NICs are not limited to the most nearshore
400 stations. In section D, for example, it is extended to a water depth of 75 m (Station D3,
401 Figure 7d). As discussed in the previous subsection, the weak NICs in the nearshore area
402 are closely related to the destruction of stratification by the strong mixing process associated
403 to the hurricane event (Yang et al., 2015; Shen et al., 2017). However, this effect does not
404 challenge the dominant role of NICs in deep waters.

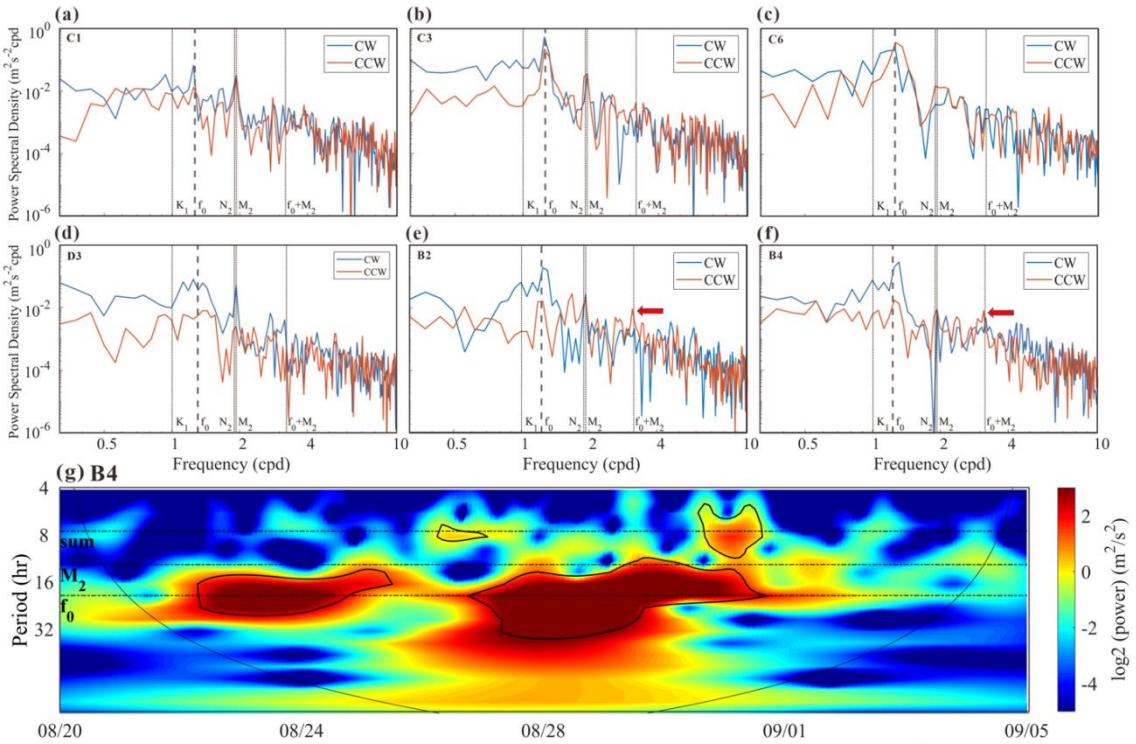

Figure 7. The rotary spectra of the current velocity in the surface layer during the simulation time (16 days) obtained by HF Radar at Stations (a) C1 (~30m), (b) C3 (~75m), (c) C6 (~1000 m), (d) D3, (e) B2 and (f) B4. Clockwise and counter-clockwise components of the current are shown by blue and orange lines, respectively (NICs are considered to be dominated by the clockwise component). The frequencies of the major tidal constituents M2, N2 and K1, the inertial frequency f0, and the sum-frequency of M2 and f_0 are all marked by gray lines. (g) Wavelet power spectrum for 10-30 m depth-averaged alongshore current component at Station B4 (see Thiebaut and Vennell (2010) for detailed description). Black contours indicate the 5% significance level against red noise and the arc line indicate the cone of influence.

Previous studies reported the nonlinear wave-wave interaction could transfer energy from the M2 tide and NIC into a wave at the sum of their frequencies (fM2). The key mechanism is the coupling between the vertical shear in NIC and the vertical velocity due to the internal tide (Davis and Xing, 2003; Hopkins et al., 2014; Shen et al., 2017; Wu et al., 2020). Though the M2 tide is rather strong in shallow waters during the hurricane event (Figure 7), nonlinear wave-wave interaction between the tidal current and the NIC could be hardly identified in most part of MAB. Nevertheless, a peak of the energy spectrum seems

to appear at the sum-frequency fM2 for the surface velocity at Stations B1 to B4, near Delmarva Peninsula (B2 and B4 were taken as examples in Figure 7e, f). The evolution of energy power at different frequencies for the middle-layer averaged (i.e., 10-30 m) currents, where the flow shear is concentrated, is further demonstrated based on wavelet analysis (Station B4 was taken as an example in Figure 7g). A peak energy at the sum-frequency fM2 is clearly identified after the hurricane passage. In fact, the subsequent Section 4.2 in this paper will show that the strongest shear is found in offshore waters between Delmarva Peninsula and New Jersey, i.e., near sections B and C (Figure 9a). Besides, Brunner and Lwiza (2020) indicated that the most prominent M2 tide in southern MAB is located off Delmarva Peninsula (near section B), according to a long-term observed data. Therefore, the vertical shear in NIC and the vertical velocity due to the M2 tide is more likely to be coupled in this region (i.e., near section B). However, this interaction only occurs in limited regions and thus would not influence the NIC evolution in most part of MAB.

4 Near Inertial Kinetic Energy

4.1 Conservation of NIKE

For description of the intensity of a NIC, the near inertial kinetic energy (NIKE) may be defined in the following way:

$$E' = \frac{1}{2}\rho_0 \left|\mathbf{u}'\right|^2 \tag{13}$$

where, $\mathbf{u}'$ is the velocity of the NIC; ρ_0 is the seawater density at the standard atmospheric pressure. Note that the NIKE is mainly gained from the wind power and dissipated due to a few mechanisms. Evolution of the vertically integrated NIKE within a water column from the sea bottom the ocean surface is thus governed by (Zhai et al., 2009)

$$\begin{aligned}\int_{-d}^{\eta} \frac{\partial E'}{\partial t} dz = \boldsymbol{\tau}_s \cdot \mathbf{u}_s' + \boldsymbol{\tau}_b \cdot \mathbf{u}_b' - \int_{-d}^{\eta} \rho_0 \nu_e \left|\frac{\partial \mathbf{u}'}{\partial z}\right|^2 dz - \\ \int_{-d}^{\eta} \nabla \cdot \left(\mathbf{u}' p'\right) dz - \int_{-d}^{\eta} \rho' g w' dz - \int_{-d}^{\eta} \nabla \cdot \left(\mathbf{U} E'\right) dz + \text{others}\end{aligned} \tag{14}$$

where, $\mathbf{u}_s'$ and $\mathbf{u}_b'$ are near inertial velocities at sea surface and bottom, respectively; $\mathbf{U}$ is the sub-inertial velocity; ρ' is the perturbation density, defined by $\rho' = \rho - \rho_*$; ρ_* is the reference density, i.e., the density corresponding to a flattened stratification where the fluid is redistributed adiabatically to a stable and vertically uniform state from the actual condition (Holliday and McIntyre, 1981; Kang and Fringer, 2010; MacCready and Giddings, 2016); p' is the perturbation pressure, defined by $p' = g\int_z^{\eta} \rho' dz$. Terms on the right-hand side of Eq. (13) are the wind energy input, the dissipation due to bottom friction, the vertical diffusion due to turbulence, the horizontal divergence of near inertial energy flux, the conversion between kinetic and potential energy, and the advection of NIKE by the sub-inertial flow. The last term 'others' includes nonlinear transfer of energy between NICs and flows of other frequencies as well as the horizontal diffusion due to mixing. Note that the energy are integrated over the water column from $z = -d$ to free surface $z = \eta$. In shallow waters, d is the actual water depth, while in deep waters, d is truncated to 200 m (i.e., the depth of the shelf break). When the bottom boundary is set at $z = -200\ \mathrm{m}$, the bottom friction vanishes in Eq. (13) but a term related to the downward energy flux, i.e., $p'w'|_{z=-200m}$ should be added.

For a general understanding, distribution of the depth-integrated NIKE averaged over a 10-day period from August 25 to September 4 is presented in Figure 8a. The wind power integrated over the same period is plotted in Figure 8b. It is clearly shown in Figure 8a that the high NIKE region mainly located in the offshore waters of Delmarva Peninsula and New Jersey rather than in the nearshore area. This distribution pattern is rather similar to that of the wind energy input, as presented in Figure 8b, indicating that the NIKE was immediately gained from the wind power (Rayson et al. 2015; Shen et al., 2017; Zhang et al., 2018). In fact, the NIKE could also come from other processes apart from the wind energy input (Alford et al, 2016), meanwhile the wind energy input may also be transferred to energy of waves apart from NIC (Chen at el., 2017), which leads to differences between Figure 8a and 7b.

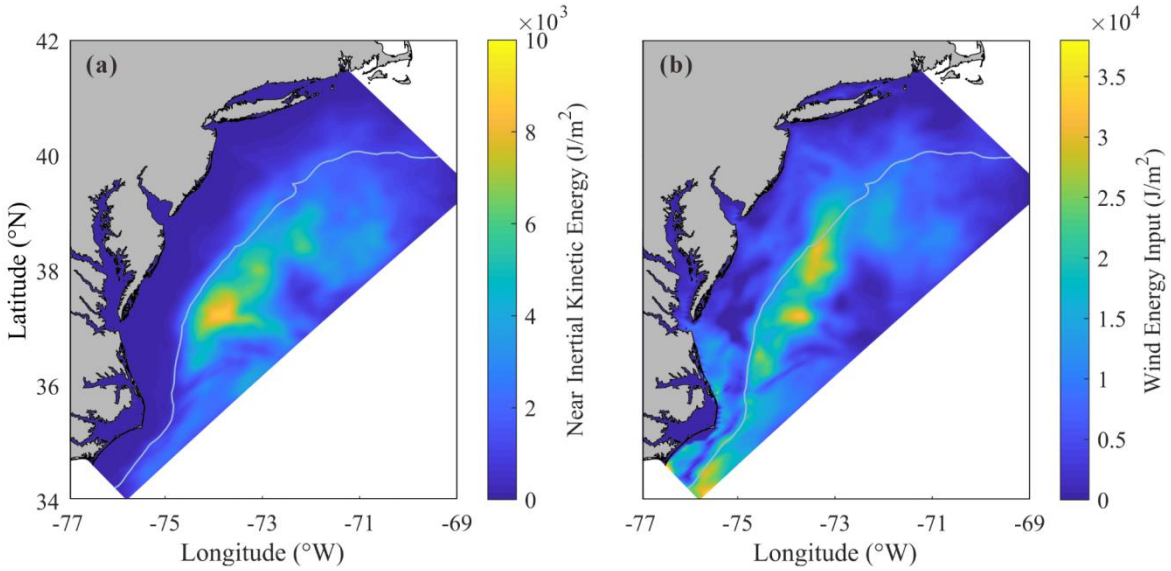

Figure 8. Spatial distribution of (a) depth-integrated near inertial kinetic energy averaged over the 10-day period and (b) wind power input to NICs integrated over the 10-day period.

Table 1. The contribution of each mechanism to energy budget. Percentages in parentheses refer to the ratio of each factor to wind energy input.

Factor (J)	Contribution in Region A	Contribution in Region B
Wind Energy Input	7.75×10^{14}	3.16×10^{14}
Vertical Turbulence Diffusion	3.12×10^{14} (40%)	2.12×10^{14} (67%)
Lateral Divergence	1.34×10^{14} (17%)	5.69×10^{13} (18%)
Downward Transfer	2.58×10^{14} (33%)	0
Advection	3.33×10^{13} (4%)	1.04×10^{13} (3%)
Conversion	6.9×10^{12} (1%)	1.58×10^{13} (5%)
Bottom Friction	0	7.58×10^{13} (24%)

An important objective of the present study is to identify the mechanism of NIC development and decay. For this purpose, we consider a rectangular domain and separate it into deep water region A (depth > 200 m) and continental shelf region B (depth $\leqslant$ 200 m), as depicted in Figure 1a. If the NICs are considered to be negligibly weak before and after

Hurricane Irene (2011), we may try to find how the wind power that drives the NICs during the hurricane event is balanced, by comparing the accumulated contribution of different mechanisms. Performing an integration of each terms in Eq. (13) with respect to time over 10 days from August 25 to September 4 and with respect to the horizontal coordinates over both deep water region A and continental shelf region B, the contribution of each mechanism to the energy budget is obtained as shown in Table 1. It is clearly demonstrated that in the deep water region, the wind energy input was basically balanced by the vertical diffusion due to turbulence (40%) and a downward transfer of the near inertial energy to the deep ocean (33%). In the continental shelf region, the vertical diffusion due to turbulence dominated the dissipation of NIKE (nearly 70%), while the bottom friction played a secondary role (24%). It is worthwhile mentioning that lateral divergence of NIKE should not be neglected in both shallow and deep water regions under the hurricane condition (nearly 20%), different from previous studies which focused on NICs under the local wind condition or in a broader research region across the whole North Atlantic (Chant, 2001; Zhai et al., 2009; Shen et al., 2017). Other processes, e.g., advection due to sub-inertial flows, only played a minor role. Note that the ratio of near inertial energy decay to wind energy input exceeded 100% in the continental shelf region, confirming that NIKE may be gained from other sources in addition to wind energy input in nearshore regions (Alford et al., 2016).

4.2 Decay of NIKE

The spatial distribution of the time-integrated energy dissipated through vertical diffusion due to turbulence is plotted in Figure 9a. It is seen that a large amount of the dissipation occurred at the offshore side of the continental shelf (i.e., at the offshore side of the shallow region B), which does not coincide with the region where the wind energy input is intense as demonstrated in Figure 8b. This implies that dissipation of NIKE is not mainly caused by an increased intensity of turbulence, which certainly takes place in a region where wind energy input achieves a high level (Zhai et al., 2009; Zhang et al., 2018). For a more detailed discussion, the averaged eddy viscosity ν_e and the averaged vertical shear rate of NIC $\left|\partial \mathbf{u}' / \partial z\right|^2$ during the period of our study are presented in Figure 9b and 8c. It is then

confirmed that the strong vertical shear also occurred at the outer half of the continental shelf. The eddy viscosity, however, has a completely different distribution. In conclusion, the vertical shear, known to be closely related to the ocean stratification (Shen et al., 2017), plays a crucial role in the turbulence diffusion. It happened that one of the well-known sharpest thermoclines in the world exists in the coastal water of MAB (Schofield et al., 2008; Lentz, 2017). It may be necessary to emphasize that, although the stratification in the shallowest water was totally destroyed during the hurricane event, as mentioned in Section 3, the seawater at the outer half of the continental shelf still partly maintained its stratification.

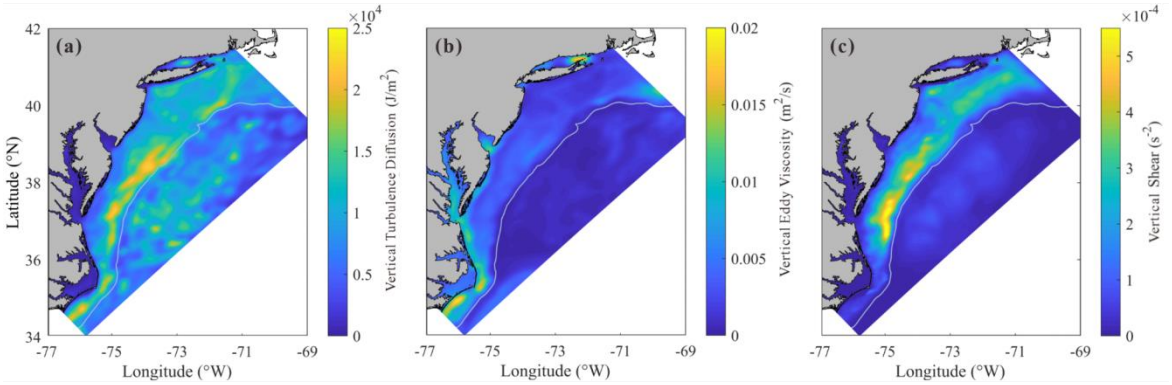

Figure 9. Spatial distribution of (a) depth-integrated vertical diffusion due to turbulence integrated over the 10-day period, (b) depth-averaged vertical eddy viscosity and (c) depth-averaged vertical shear, both averaged over the 10-day period.

The lateral divergence of NIKE flux, which also results in decay of NIKE and is not trivial (~20%) in both shallow and deep water regions, may have to be discussed in some details. As shown in Eq. (13), the lateral divergence of NIKE flux is a vertical integration of $\nabla\cdot\ \mathbf{u}'p'$, which may also be expressed as an equivalent integration of $\nabla\cdot(\mathbf{c}'E')$, where $\mathbf{c}'$ is the transport velocity of NIKE in the horizontal plane (Price, 1994). When compared to previous studies (Zhai et al., 2009), which dealt with the normal wind induced NIC over a large part of the North Atlantic and showed that the lateral divergence accounted only for less than 5% of the total NIKE loss, we focused only on the hurricane-affected region. In the hurricane-affected region, the larger NIKE gradient naturally leads to a larger divergence. If we extend the domain of study by a factor of 1.5, however, contribution of

the averaged lateral divergence decreases by more than half. It is thus strongly implied that the lateral divergence of NIKE flux is significant within the hurricane-affected region.

It is also of interest to note that the contribution of the lateral divergence in south region of our computational domain is less than 8%, much smaller than the average value of ~20%. Several studies have pointed out that the transport velocity $\mathbf{c}'$ is largely influenced by the background vorticity gradient (Zhai et al., 2009; Park et al., 2009). In other words, NIKE can hardly be transferred from a place of lower background vorticity to a place of higher background vorticity or, NIKE can hardly penetrate a vorticity ridge from either side. Shown in Figure 10 is the distribution of the background vorticity within our computational domain during the hurricane event (data from https://resources.marine.copernicus.eu/product-detail/SEALEVEL_GLO_PHY_CLIMATE_L4_MY_008_057/INFORMATION). A remarkable vorticity ridge exists in the southeast of the computational domain, which is considered to be caused by the strong horizontal shear at the edge of Gulf Stream (a warm and swift ocean current in Atlantic, flowing through the southern MAB and propagating northeastward). This vorticity ridge can reduce the lateral divergence of NIKE flux in south region of our computational domain.

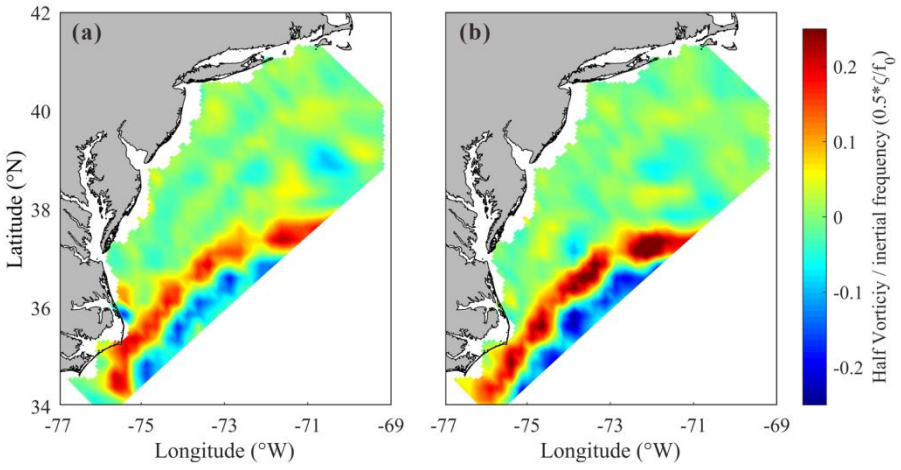

Figure 10. Spatial distribution of background vorticity (a) before the hurricane event on Aug 25 and (b) after the hurricane event on Sep 4.

4.3 Decay timescale of NIKE

It is of practical importance to determine the rate of NIKE decay. A conventional measure of the rate of NIKE may be its e-folding time, i.e., the timescale in which the NIKE decreases by a factor of e. Shown in Figure 11 is the e-folding time of the depth-integrated NIKE at 24 stations along sections A to D. The decay timescale in section E is not considered because this section is relatively far from the hurricane track as compared with other sections and also because the orientation of section E differs quite significantly from that of other sections.

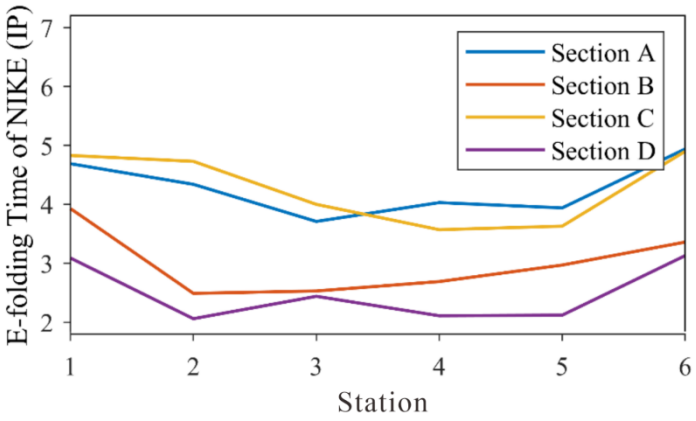

Figure 11. The decay timescale of the depth-integrated NIKE at 24 stations along sections A to D. Note that the unit for the e-folding time is the inertial period.

It is interesting to note that the decay timescales in the shallow and deep regions are fairly different. As shown in Figure 11, the NIKE is dissipated much more slowly outside the shelf break (Station No.6) than over the continental shelf. This difference is often considered to be an effect of the bottom friction and the extremely strong turbulence in the shallow waters, as pointed out by other researchers (Rayson et al., 2015; Shen et al., 2017). It is also interesting to find that the variation of NIKE decay rate in shallow waters is much more complicated than in the deep waters. In the cross-shore direction, the NIKE at the middle stations, i.e., Stations No. 3 to No. 5, located at the outer half of the continental shelf, is shown to be dissipated most rapidly, especially along sections A to C (Figure 11). This phenomenon is actually supported by the fact that the strongest turbulence diffusion

occurred over the outer half of the continental shelf, particularly in the relevant region between sections A and C (Figure 9a). Considering the variation of the wind energy input within the same section should not be too large, the ratio of turbulence diffusion to wind energy input must be mainly determined by the turbulence diffusion. Therefore, the strong turbulence dissipation due to the strong vertical shear in well-maintained stratification is responsible for the rapid energy decay in the outer half of the continental shelf, as shown in Section 4.2. Although the bottom friction also has some effect on the decay timescale of NIKE onshore, the turbulence effect is predominant.

In the alongshore direction, it is shown that the NIKE in sections B and D decayed more rapidly. Actually, the decay timescale there is only 2 to 3 inertial periods compared to 4 to 5 inertial periods in sections A and C. However, the limited variability of the turbulence diffusion in alongshore direction should not lead to such a big difference. Near section A, the vorticity ridge in Gulf Stream restricted the lateral divergence of NIKE, which may contribute to a long decay timescale to some extent. However, the role of this effect was limited. In fact, as mentioned in Section 3, the nonlinear wave-wave interaction near section B may have caused a transfer of NIKE to other frequencies, as also pointed out by Shen et al. (2017). In fact, it is found that the ratio of turbulence diffusion to wind input in section B was larger than in other sections by 20%-30%, due to the low level of wind input (Figure 8b) and high level of turbulence dissipation (Figure 9a) there. These factors combined seem to have yielded an extraordinarily short e-folding time in section B. In section D, due to the complete destruction of stratification after the hurricane event (as mentioned in Section 3 and shown in Figure 7d), the NICs were of the same order as the background flow (D1-D4 in Figure 6). Therefore, the decay timescale of NIKE in section D is certainly inaccurate and possibly meaningless.

5 Conclusion

This study is aimed to investigate the development and decay mechanism of NICs in the MAB area caused by Hurricane Irene (2011). Numerical results obtained with ROMS

607 are shown to agree well with the observational data. Both computational and observational
608 results show that the rotating wind of the hurricane immediately forced a rotating current in
609 the surface layer of the ocean and induced an inertial current rotating in the opposite
610 direction about one inertial period after the hurricane passed over. The NICs overwhelmed
611 M2 tide in most areas of the MAB region except in the nearshore area where the
612 stratification was totally destroyed by the strong mixing due to turbulence. In addition, the
613 cross-shore component of the NIC velocity gradually increases by a factor of at least three
614 from a shallow-water position to the shelf break.

615 The energy budget in the NICs is investigated in both deep and shallow waters. NIKE
616 was shown to be immediately gained from the wind power during the hurricane event. In
617 the deep water region, NIKE was mainly dissipated by the vertical diffusion due to
618 turbulence and partially transferred to deep waters. In the continental shelf region, NIKE
619 was basically dissipated by the turbulence diffusion, meanwhile the bottom friction played
620 a secondary role. The nonlinear wave-wave interaction only dissipated NIKE in limited
621 regions, e.g. shelf waters off Delmarva Peninsula. Notably, the lateral divergence of NIKE
622 should be taken into consideration in both shallow and deep water regions under the
623 hurricane condition. However, in southern MAB, it was restricted by a vorticity ridge at the
624 edge of Gulf Stream. It is also clarified that the NIKE dissipation due to turbulence diffusion
625 is much more closely related to the rate of the vertical shear rather than the intensity of
626 turbulence, which certainly takes place in a region where wind energy input achieves a high
627 level. The strong vertical shear at the offshore side of the continental shelf leaded to the
628 strong turbulence dissipation in this region.

629 ## Acknowledgements

630 This research is supported by National Natural Science Foundation of China (NSFC)
631 under grant No. 11732008.

Data Availability Statements

The data used in this study are listed below. In particular, the regional oceanic modeling system (ROMS) code is available at https://www.myroms.org; HF radar data is available at http://tds.marine.rutgers.edu/thredds/dodsC/cool/codar/totals/5Mhz_6km_realtime_fmrc/Maracoos_5MHz_6km_Totals-FMRC_best.ncd.html; Glider data is available at http://tds.marine.rutgers.edu/thredds/dodsC/cool/glider/mab/Gridded/20110810T1330_epa_ru16_active.nc.html; HYCOM data is available at https://www.hycom.org/data/glbu0pt08/expt-91pt2; ADCIRC data is available at https://adcirc.org/products/adcirc-tidal-databases; USGS data is available at https://waterdata.usgs.gov; H*WIND data is available at https://www.aoml.noaa.gov/hrd/data_sub/wind.html; NAM data is available at https://www.ncdc.noaa.gov/data-access/model-data/model-datasets/north-american-mesoscale-forecast-system-nam; C3S data is available at https://resources.marine.copernicus.eu/product-detail/SEALEVEL_GLO_PHY_CLIMATE_L4_MY_008_057/INFORMATION; AVHRR data is available at https://earth.esa.int/eogateway/catalog/avhrr-level-1b-local-area-coverage-imagery.

References

Alford, M.H., 2003a. Improved global maps and 54-year history of wind-work on ocean inertial motions. Geophysical Research Letters, 30(8).

Alford, M.H., 2003b. Redistribution of energy available for ocean mixing by long-range propagation of internal waves. Nature, 423(6936): 159-162.

Alford, M.H., MacKinnon, J.A., Simmons, H.L. and Nash, J.D., 2016. Near-inertial internal gravity waves in the ocean. Annual Review of Marine Science, 8(1): 95-123.

Allahdadi, M., 2014. Numerical experiments of hurricane impact on vertical mixing and de-stratification of the louisiana shelf waters. Ph. D. Thesis, Louisiana State University, Baton Rouge.

Amante, C. and Eakins, B.W., 2009. Etopo1 1 arc-minute global relief model: Procedures, data sources and analysis. NOAA Technical Memorandum NESDIS NGDC-24,

National Geophysical Data Center, NOAA.

Avila, L.A. and Cangialosia, J., 2011. Tropical cyclone report: Hurricane irene: August 21–28, 2011. National Hurricane Center Report AL0920011, US National Oceaninc and Atmospheric Administration's National Weather Service.

Brunner, K. and Lwiza, K.M.M., 2020. Tidal velocities on the mid-atlantic bight continental shelf using high-frequency radar. Journal of Oceanography, 76(4): 289-306.

Castelao, R.M., 2014. Mesoscale eddies in the south atlantic bight and the gulf stream recirculation region: Vertical structure. Journal of Geophysical Research: Oceans, 119(3): 2048-2065.

Chang, S.W. and Anthes, R.A., 1978. Numerical simulations of the ocean's nonlinear, baroclinic response to translating hurricanes. Journal of Physical Oceanography, 8(3): 468-480.

Chant, R.J., 2001. Evolution of near-inertial waves during an upwelling event on the new jersey inner shelf. Journal of Physical Oceanography, 31(3): 746-764.

Chassignet, E.P. et al., 2007. The hycom (hybrid coordinate ocean model) data assimilative system. Journal of Marine Systems, 65(1): 60-83.

Chen, C., Reid, R.O. and Nowlin Jr, W.D., 1996. Near-inertial oscillations over the texas-louisiana shelf. Journal of Geophysical Research: Oceans, 101(C2): 3509-3524.

Chen, C. and Xie, L., 1997. A numerical study of wind-induced, near-inertial oscillations over the texas-louisiana shelf. Journal of Geophysical Research: Oceans, 102(C7): 15583-15593.

Chen, G., Xue, H., Wang, D. and Xie, Q., 2013. Observed near-inertial kinetic energy in the northwestern south china sea. Journal of Geophysical Research: Oceans, 118(10): 4965-4977.

Chen, S., Chen, D. and Xing, J., 2017. A study on some basic features of inertial oscillations and near-inertial internal waves. Ocean Science, 13(5): 829-836.

Chen, Y. and Yu, X., 2016. Enhancement of wind stress evaluation method under storm conditions. Climate Dynamics, 47(12): 3833-3843.

687 Chen, Y., Zhang, F., Green, B.W. and Yu, X., 2018. Impacts of ocean cooling and reduced
688 wind drag on hurricane katrina (2005) based on numerical simulations. Monthly
689 Weather Review, 146(1).
690 Churchill, J.H., Wirick, C.D., Flagg, C.N. and Pietrafesa, L.J., 1994. Sediment resuspension
691 over the continental shelf east of the delmarva peninsula. Deep Sea Research Part II:
692 Topical Studies in Oceanography, 41(2): 341-363.
693 Cummings, J.A., 2005. Operational multivariate ocean data assimilation. Quarterly Journal
694 of the Royal Meteorological Society, 131(613): 3583-3604.
695 D'Asaro, E.A., 1985. The energy flux from the wind to near-inertial motions in the surface
696 mixed layer. Journal of Physical Oceanography, 15: 1043-1059.
697 Davies, A.M. and Xing, J., 2003. On the interaction between internal tides and wind-induced
698 near-inertial currents at the shelf edge. Journal of Geophysical Research: Oceans,
699 108(C3).
700 Derrick, T.R., Bates, B.T. and Dufek, J.S., 1994. Evaluation of time-series data sets using
701 the pearson product-moment correlation coefficient. Medicine and science in sports
702 and exercise, 26(7): 919-928.
703 Donelan, M.A. et al., 2004. On the limiting aerodynamic roughness of the ocean in very
704 strong winds. Geophysical Research Letters, 31(18).
705 Dorostkar, A., Boegman, L., Diamessis, P. and Pollard, A., 2010. Sensitivity of mitgcm to
706 different model parameters in application to cayuga lake. Proceedings of the 6th
707 International Symposium on Environmental Hydraulics, Two Volume Set, p.^pp.
708 373-378.
709 Emanuel, K.A., 1995. Sensitivity of tropical cyclones to surface exchange coefficients and
710 a revised steady-state model incorporating eye dynamics. Journal of the
711 Atmospheric Sciences, 52: 3969-3976.
712 Fairall, C.W., Bradley, E.F., Rogers, D.P., Edson, J.B. and Young, G.S., 1996. Bulk
713 parameterization of air-sea fluxes for tropical ocean-global atmosphere coupled-
714 ocean atmosphere response experiment. Journal of Geophysical Research: Oceans,

101(C2): 3747-3764.

Freeman, N.G., Hale, A.M. and Danard, M.B., 1972. A modified sigma equations' approach to the numerical modeling of great lakes hydrodynamics. Journal of Geophysical Research 77(6): 1050-1060.

Furuichi, N., Hibiya, T. and Niwa, Y., 2008. Model-predicted distribution of wind-induced internal wave energy in the world's oceans. Journal of Geophysical Research: Oceans, 113(C9).

Garrett, C., 2001. What is the “near-inertial” band and why is it different from the rest of the internal wave spectrum? Journal of Physical Oceanography, 31(4): 962-971.

Glenn, S.M. et al., 2016. Stratified coastal ocean interactions with tropical cyclones. Nature Communications, 7(1): 10887.

Gregg, M.C., 1987. Diapycnal mixing in the thermocline: A review. Journal of Geophysical Research: Oceans, 92(C5): 5249-5286.

Haidvogel, D.B. et al., 2008. Ocean forecasting in terrain-following coordinates: Formulation and skill assessment of the regional ocean modeling system. Journal of Computational Physics, 227(7): 3595-3624.

Hoarfrost, A. et al., 2019. Gulf stream ring water intrusion on the mid-atlantic bight continental shelf break affects microbially driven carbon cycling. 6.

Holliday, D. and McIntyre, M.E., 1981. On potential energy density in an incompressible, stratified fluid. Journal of Fluid Mechanics, 107: 221-225.

Hopkins, J.E., Stephenson Jr, G.R., Green, J.A.M., Inall, M.E. and Palmer, M.R., 2014. Storms modify baroclinic energy fluxes in a seasonally stratified shelf sea: Inertial-tidal interaction. Journal of Geophysical Research: Oceans, 119(10): 6863-6883.

Hormann, V., Centurioni, L.R., Rainville, L., Lee, C.M. and Braasch, L.J., 2014. Response of upper ocean currents to typhoon fanapi. Geophysical Research Letters, 41(11): 3995-4003.

Jackett, D.R. and McDougall, T.J., 1995. Minimal adjustment of hydrographic profiles to achieve static stability. Journal of Atmospheric and Oceanic Technology, 12(2): 381-

389.

Janjic, Z.I. et al., 2004, June. The ncep wrf core, 20th Conference on Weather Analysis and Forecasting/16th Conference on Numerical Weather Prediction, Seattle, Washington, pp. 10-25.

Jochum, M. et al., 2013. The impact of oceanic near-inertial waves on climate. Journal of Climate, 26(9): 2833-2844.

Kang, D. and Fringer, O., 2010. On the calculation of available potential energy in internal wave fields. Journal of Physical Oceanography, 40(11): 2539-2545.

Kawaguchi, Y., Wagawa, T. and Igeta, Y., 2020. Near-inertial internal waves and multiple-inertial oscillations trapped by negative vorticity anomaly in the central sea of japan. Progress in Oceanography, 181: 102240.

Kim, S.Y. and Kosro, P.M., 2013. Observations of near-inertial surface currents off oregon: Decorrelation time and length scales. Journal of Geophysical Research: Oceans, 118(7): 3723-3736.

Kohut, J., Roarty, H., Randall-Goodwin, E., Glenn, S. and Lichtenwalner, C.S., 2012. Evaluation of two algorithms for a network of coastal HF Radars in the Mid-Atlantic Bight. Ocean Dynamics, 62(6): 953-968.

Kunze, E., 1985. Near-inertial wave propagation in geostrophic shear. Journal of Physical Oceanography, 15(5): 544-565.

Lentz, S.J., 2017. Seasonal warming of the middle atlantic bight cold pool. Journal of Geophysical Research: Oceans, 122(2): 941-954.

Li, M., Zhong, L., Boicourt, W.C., Zhang, S. and Zhang, D.-L., 2007. Hurricane-induced destratification and restratification in a partially-mixed estuary. Journal of Marine Research, 65(2): 169-192.

MacCready, P. and Giddings, S.N., 2016. The mechanical energy budget of a regional ocean model. Journal of Physical Oceanography, 46(9): 2719-2733.

MacKinnon, J.A. and Gregg, M.C., 2005. Near-inertial waves on the new england shelf: The role of evolving stratification, turbulent dissipation, and bottom drag. Journal

771 of Physical Oceanography, 35(12): 2408-2424.
772 Marchesiello, P., McWilliams, J.C. and Shchepetkin, A., 2001. Open boundary conditions
773 for long-term integration of regional oceanic models. Ocean Modelling, 3(1): 1-20.
774 Miles, T., Seroka, G. and Glenn, S., 2017. Coastal ocean circulation during hurricane sandy.
775 Journal of Geophysical Research: Oceans, 122(9): 7095-7114.
776 Mulligan, R.P. and Hanson, J.L., 2016. Alongshore momentum transfer to the nearshore
777 zone from energetic ocean waves generated by passing hurricanes. Journal of
778 Geophysical Research: Oceans, 121(6): 4178-4193.
779 Munk, W. and Wunsch, C., 1998. Abyssal recipes ii: Energetics of tidal and wind mixing.
780 Deep Sea Research Part I: Oceanographic Research Papers, 45(12): 1977-2010.
781 Olabarrieta, M., Warner, J.C. and Kumar, N., 2011. Wave-current interaction in willapa bay.
782 Journal of Geophysical Research: Oceans, 116(C12).
783 Park, J.J., Kim, K. and Schmitt, R.W., 2009. Global distribution of the decay timescale of
784 mixed layer inertial motions observed by satellite-tracked drifters. Journal of
785 Geophysical Research: Oceans, 114(C11).
786 Pollard, R.T., 1980. Properties of near-surface inertial oscillations. Journal of Physical
787 Oceanography, 10(3): 385-398.
788 Powell, M.D., Houston, S.H., Amat, L.R. and Morisseau-Leroy, N., 1998. The hrd real-time
789 hurricane wind analysis system. Journal of Wind Engineering and Industrial
790 Aerodynamics, 77-78: 53-64.
791 Powell, M.D., Vickery, P.J. and Reinhold, T.A., 2003. Reduced drag coefficient for high
792 wind speeds in tropical cyclones. Nature, 422(6929): 279-283.
793 Price, J.F., 1983. Internal wave wake of a moving storm. Part i. Scales, energy budget and
794 observations. Journal of Physical Oceanography, 13(6): 949-965.
795 Price, J.F., Sanford, T.B. and Forristall, G.Z., 1994. Forced stage response to a moving
796 hurricane. Journal of Physical Oceanography, 24(2): 233-260.
797 Rayson, M.D. et al., 2015. Near-inertial ocean response to tropical cyclone forcing on the
798 australian north-west shelf. Journal of Geophysical Research: Oceans, 120(12):

799 7722-7751.
800 Rimac, A., von Storch, J.-S., Eden, C. and Haak, H., 2013. The influence of high-resolution
801 wind stress field on the power input to near-inertial motions in the ocean.
802 Geophysical Research Letters, 40(18): 4882-4886.
803 Roarty, H. et al., 2010. Operation and application of a regional high-frequency radar
804 network in the mid-atlantic bight. Marine Technology Society Journal, 44(6): 133-
805 145.
806 Roarty, H. et al., 2020. Annual and seasonal surface circulation over the mid-atlantic bight
807 continental shelf derived from a decade of high frequency radar observations.
808 Journal of Geophysical Research: Oceans, 125(11): e2020JC016368.
809 Rodi, W., 1987. Examples of calculation methods for flow and mixing in stratified fluids.
810 Journal of Geophysical Research: Oceans, 92(C5): 5305-5328.
811 Sanford, T.B., Price, J.F. and Girton, J.B., 2011. Upper-ocean response to hurricane frances
812 (2004) observed by profiling em-apex floats. Journal of Physical Oceanography,
813 41(6): 1041-1056.
814 Schofield, O. et al., 2008. The decadal view of the mid-atlantic bight from the coolroom: Is
815 our coastal system changing? Oceanography, 21(4): 108-117.
816 Schofield, O. et al., 2007. Slocum gliders: Robust and ready. Journal of Field Robotics,
817 24(6): 473-485.
818 Schofield, O. et al., 2010. A regional slocum glider network in the Mid-Atlantic Bight
819 leverages broad community engagement. Marine Technology Society Journal, 44(6):
820 185-195.
821 Seroka, G. et al., 2016. Hurricane Irene sensitivity to stratified coastal ocean cooling.
822 Monthly Weather Review, 144(9): 3507-3530.
823 Seroka, G. et al., 2017. Rapid shelf-wide cooling response of a stratified coastal ocean to
824 hurricanes. Journal of Geophysical Research: Oceans, 122(6): 4845-4867.
825 Shchepetkin, A.F. and McWilliams, J.C., 2005. The regional oceanic modeling system
826 (roms): A split-explicit, free-surface, topography-following-coordinate oceanic

827 model. Ocean Modelling, 9(4): 347-404.
828 Shearman, R.K., 2005. Observations of near-inertial current variability on the new england
829 shelf. Journal of Geophysical Research: Oceans, 110(C2).
830 Shen, J., Qiu, Y., Zhang, S. and Kuang, F., 2017. Observation of tropical cyclone-induced
831 shallow water currents in taiwan strait. Journal of Geophysical Research: Oceans,
832 122(6): 5005-5021.
833 Steiner, A. et al., 2017. Critical weather situations for renewable energies-part a: Cyclone
834 detection for wind power. Renewable Energy, 101: 41-50.
835 Stommel, H., 2020. The Gulf Stream. University of California Press.
836 Thiebaut, S. and Vennell, R., 2010. Observation of a fast continental shelf wave generated
837 by a storm impacting newfoundland using wavelet and cross-wavelet analyses.
838 Journal of Physical Oceanography, 40(2): 417-428.
839 Thyng, K.M. et al., 2021. Performance of offline passive tracer advection in the regional
840 ocean modeling system (roms; v3.6, revision 904). Geoscientific Model
841 Development, 14(1): 391-407.
842 Toffoli, A., McConochie, J., Ghantous, M., Loffredo, L. and Babanin, A.V., 2012. The effect
843 of wave-induced turbulence on the ocean mixed layer during tropical cyclones: Field
844 observations on the australian north-west shelf. Journal of Geophysical Research:
845 Oceans, 117(C11).
846 Umlauf, L. and Burchard, H., 2003. A generic length-scale equation for geophysical
847 turbulence models. Journal of Marine Research, 61(2): 235-265.
848 Warner, J.C., Defne, Z., Haas, K. and Arango, H.G., 2013. A wetting and drying scheme for
849 roms. Computers & Geosciences, 58: 54-61.
850 Wu, R., Zhang, H. and Chen, D., 2020. Effect of typhoon kalmaegi (2014) on northern south
851 china sea explored using muti-platform satellite and buoy observations data.
852 Progress in Oceanography, 180: 102218.
853 Xu, J., Chao, S.-Y., Hood, R.R., Wang, H.V. and Boicourt, W.C., 2002. Assimilating high-
854 resolution salinity data into a model of a partially mixed estuary. Journal of

Geophysical Research: Oceans, 107(C7): 11-1-11-14.

Xu, Y. and Yu, X., 2021. Enhanced atmospheric wave boundary layer model for evaluation of wind stress over waters of finite depth. Progress in Oceanography, 198: 102664.

Yang, B., Hou, Y., Hu, P., Liu, Z. and Liu, Y., 2015. Shallow ocean response to tropical cyclones observed on the continental shelf of the northwestern south china sea. Journal of Geophysical Research: Oceans, 120(5): 3817-3836.

Zhai, X., Greatbatch, R.J., Eden, C. and Hibiya, T., 2009. On the loss of wind-induced near-inertial energy to turbulent mixing in the upper ocean. Journal of Physical Oceanography, 39(11): 3040-3045.

Zhang, F., Li, M. and Miles, T., 2018. Generation of near-inertial currents on the Mid-Atlantic Bight by Hurricane Arthur (2014). Journal of Geophysical Research: Oceans, 123(4): 3100-3116.

Zhang, H. et al., 2016. Upper ocean response to Typhoon Kalmaegi (2014). Journal of Geophysical Research: Oceans, 121(8): 6520-6535.